remote sensing

MDPI

Article

Retrieval and Spatio-Temporal Variations Analysis of Yangtze River Water Clarity from 2017 to 2020 Based on Sentinel-2 Images

Yelong Zhao [1,2], Shenglei Wang [2], Fangfang Zhang [2,*], Qian Shen [2] and Junsheng Li [2,3,4]

1 School of Geomatics, Liaoning Technical University, Fuxin 123000, China; 471710035@lntu.edu.cn
2 Key Laboratory of Digital Earth Science, Aerospace Information Research Institute, Chinese Academy of Sciences, Beijing 100049, China; wangsl@radi.ac.cn (S.W.); shenqian@radi.ac.cn (Q.S.); lijs@radi.ac.cn (J.L.)
3 Key Laboratory of Earth Observation Hainan Province, Sanya 572029, China
4 School of Electronic, Electrical and Communication Engineering, University of Chinese Academy of Sciences, Beijing 100049, China
* Correspondence: zhangff07@radi.ac.cn; Tel.: +86-137-1765-5892

Abstract: The Yangtze River is the third longest river in the world. Monitoring and protecting its water quality are important for economic and social development. Water clarity (Secchi disk depth, SDD) is an important reference index for evaluating water quality. In this study, Sentinel-2 multispectral instrument (MSI) remote sensing images were utilized together with the Forel-Ule index (FUI) and hue angle α to construct an SDD retrieval model, which was applied to the Yangtze River from 2017 to 2020, which was used to describe color in the International Commission on Illumination (CIE) color space to construct an SDD retrieval model that was applied to the Yangtze River for the period 2017–2020. Further, the spatial distribution, seasonal variation, inter-annual variation, and driving factors of the observed SDD variations were analyzed. The spatial distribution pattern of the Yangtze River was high in the west and low in the east. The main driving factors affecting the Yangtze River SDD was sediment runoff, water level, and precipitation. The upstream and downstream Yangtze River SDD were negatively correlated with the change in water level and sediment runoff, whereas the midstream Yangtze River SDD was positively correlated with the change in water level and sediment runoff. The upper and lower reaches of the Yangtze River and overall SDD showed a weak downward trend, and the middle reaches of the Yangtze River remained almost unchanged.

Keywords: Secchi disk depth; Forel-Ule Index; hue angle; Sentinel-2; Yangtze River

Citation: Zhao, Y.; Wang, S.; Zhang, F.; Shen, Q.; Li, J. Retrieval and Spatio-Temporal Variations Analysis of Yangtze River Water Clarity from 2017 to 2020 Based on Sentinel-2 Images. *Remote Sens.* **2021**, *13*, 2260. https://doi.org/10.3390/rs13122260

Academic Editor: SeungHyun Son

Received: 10 April 2021
Accepted: 2 June 2021
Published: 9 June 2021

1. Introduction

Surface water is an important resource for daily human life and industrial production; hence, its quality is closely related to human production and life. The Yangtze River is the third largest river in the world, and it is also an important water resource for coastal residents. It has many water conservancy projects, such as the Three Gorges Project and the Middle Route Project of South to North Water Diversion. The main stream of the Yangtze River runs through 11 provinces (municipalities, autonomous regions) in China from west to east and is the most abundant river in China. Because the Yangtze River plays a very important role in social development in China, it is necessary to protect and monitor the water quality of the Yangtze River [1].

Water clarity (Secchi disk depth: SDD) is the most commonly used index for evaluating water quality. Scholars worldwide have utilized this index for water environment management and monitoring [2–6]. It is widely employed to obtain water depth by measuring the depth of the Secchi disk in water and has the advantages of simplicity and convenience [7,8]. However, extensive field survey work is required, which entails high

labor and time costs, low efficiency, and the inability to obtain real-time dynamic variations in water bodies. In contrast, remote sensing technology has the advantages of wide monitoring range, rapid information acquisition, short measurement period, and intuitive information, and long-term series change of large-scale water areas can be monitored using multi-source remote sensing data [9,10].

An empirical algorithm involving band combination based on Landsat remote sensing images has been successfully employed to obtain water clarity of inland water [7,11,12]. The TM1 and TM3 bands of Landsat 4 or 5 remote sensing images have been used to monitor the 20-year long-term series of water clarity of 10,500 lakes in Minnesota, USA [4]. The B4 and B3 bands of Landsat 8 remote sensing images have been used to retrieve the water clarity of the Three Gorges Reservoir and Dongting Lake in China, as well as the relationship between the Three Gorges Dam and the Three Gorges Reservoir and Dongting Lake [13]. The water clarity of the three lakes in Northeast China was evaluated using Landsat 7 remote sensing images according to four regression equations, and the results showed that the water clarity of the lakes in this region had a strong geographical pattern [14]. Lathrop and Lillesand used the green band of Landsat 4 or 5 remote sensing images to retrieve the water clarity of Southern Green Bay and Central Lake Michigan of WI, USA [15]. Further, Lathrop utilized Landsat 4 or 5 remote sensing images to compare the retrieval results of Michigan lake, Yellowstone Lake, and Jackson Lake [16]. The ratio between the blue and green bands of Landsat TM remote sensing images was used to estimate the water clarity of Iseo Lake, Italy [17]. Thirteen Landsat MSS and TM remote sensing images were employed to analyze the spatial distribution pattern and temporal change trends of more than 500 lakes with water areas greater than 10 ha in Minneapolis and St. Paul [18,19]. The red band of the Landsat TM remote sensing images was utilized to estimate the water clarity of New York Harbor [20].

Lee and Doron et al. proposed an analysis model using a moderate-resolution imaging spectroradiometer (MODIS) and medium-resolution imaging spectrometer (MERIS) and selected the appropriate band to invert the vertical attenuation coefficient and transmittance depth product [9,21,22]. It has been proven that there is a strong correlation between SDD and single-band reflectivity [7,23,24]. The 555-nm water leaving radiance of the sea viewing wide field-of-view (SeaWiFS) sensor was used to study the time series changes of Canadian waters between 1997 and 2001, and the researchers emphasized that the Great Lakes region is worthy of further study on important features on a larger time scale [25]. Shi et al. [26] used the R (645 nm) band of MODIS data to retrieve the data for Taihu Lake and performed long time series analysis.

Although scholars have researched the water quality of the Yangtze River, there has been no time-series analysis of the Yangtze River based on high-resolution remote sensing satellite data [13,27–37]. Owing to the wide distribution of the Yangtze River, the complexity and dynamic variability of the optical properties of inland water remain obstacles to the application of the aforementioned empirical and analytical models in a wide range of optical water types, and the Fore-Ule index (FUI) and hue angle α strongly interfere with the aerosol types and observation conditions. Therefore, the work of Wang et al. was referenced in this study to retrieve the SDD from the FUI and hue angle α [6]. The model was applied to Sentinel-2 remote sensing images to calculate the spatial distribution pattern and seasonal and interannual changes in the SDD of the main stream of the Yangtze River (Yibin City, Sichuan Province to the estuary) from 2017 to 2020. Sentinel-2 remote sensing images have significant application potential in the field of water science [38–41]. Sentinel-2A/2B complement each other, enabling the reply time to be shortened to 5 days and more suitable remote sensing images to be screened every month. Additionally, the revisit time of the twin Sentinel-2 satellites reaches 2–3 days in the mid-latitudes. A spatial resolution of 10 m can satisfy the requirement of a large number of available pixels in the upper, middle, lower reaches, and estuary of the Yangtze River. Therefore, Sentinel-2 data were selected as the remote sensing data to analyze the main stream of the Yangtze River, as they possess sufficient reply time and spatial resolution. Finally, the Yangtze River

SDD results retrieved from the Sentinel-2 remote sensing images were correlated with the environmental and human factors that may affect the changes in the Yangtze River SDD. Among them, the natural factors are precipitation, sediment runoff, and water level; the main human factors are the construction of reservoirs along the way and the discharge of pollutants.

2. Area and Data

2.1. Study Area

The main stream of the Yangtze River runs through Western China from west to east, between 90°33′–122°25′ E and 24°30′–35°45′ N, corresponding to the entire basin [1]. Above Yichang City, Hubei Province is the upper reaches of the Yangtze River, with a length of 4504 km, drainage area of 100 km^2, river width of 0.5–1.5 km, and water depth of 5–20 m. Traditionally, that section is called the upper reaches of the Yangtze River; and the section from Yichang City, Hubei Province to Hukou County of Jiujiang City, Jiangxi Province is called the middle reaches of the Yangtze River, with a length of 955 km, drainage area of 680,000 km^2, river width of 1–2 km, and water depth of 6–15 m; Hukou County of Jiujiang City, Jiangxi Province to estuary is called the lower reaches of the Yangtze River, with a length of 938 km, drainage area of 120,000 km^2, a river width of 2–4 km, a water depth of 10–20 m, and a river width of more than 15 km [42,43]. Figure 1 shows the research area of this study.

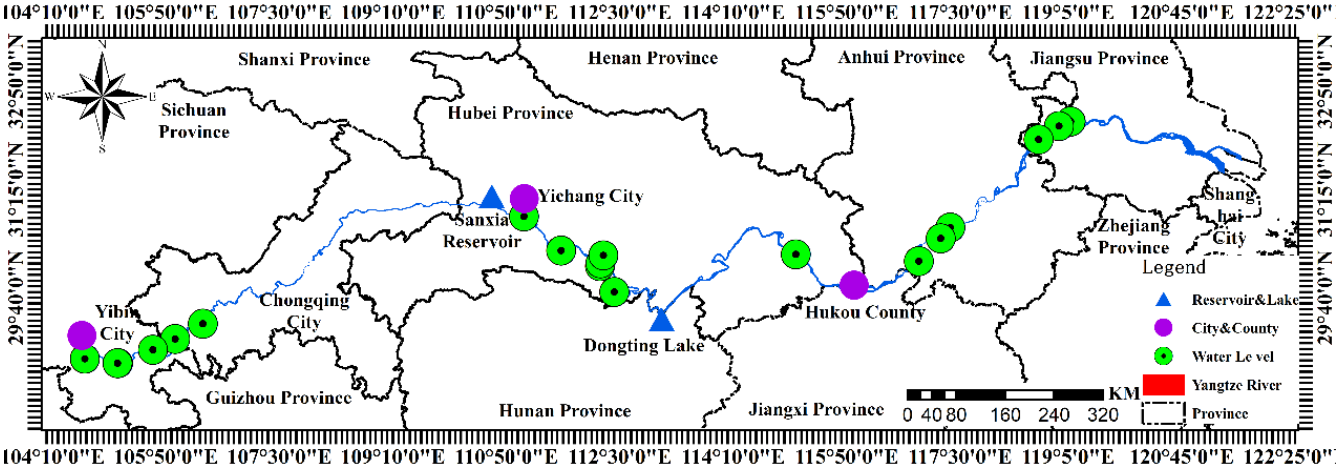

Figure 1. Study area.

2.2. Sentinel-2 MSI Data

Sentinel-2 is a high-resolution multispectral satellite with an orbit height of 786 km, a width of 290 km, 13 bands, and spatial resolutions of 10, 20, and 60 m. Sentinel-2A and Sentinel-2B were launched in June 2015 and March 2017, respectively. The reply time of each satellite is 10 days. The two satellites complement each other, and the reply time is shortened to 5 days. The data processing in this study was conducted on the Google Earth Engine (GEE) platform and locally. We downloaded the level 1C top of atmosphere (L1C TOA) data from 2017 to 2018 from the European Space Agency (ESA) website. We used the Sen2Cor and SNAP software developed by ESA to conduct atmospheric correction and band resampling on the L1C TOA data and finally obtained the surface reflectance data with a spatial resolution of 10 m in each band. Based on the surface reflectance data, the results of SDD of the Yangtze River from 2017 to 2018 were calculated. The widths of the upper, middle, and lower reaches of the Yangtze River and the estuary are 0.5–1.5, 1–2, 2–4, and >15 km, respectively. Owing to the large difference of river width in the upper, middle, lower reaches, and estuary of the Yangtze River, the selection of remote sensing data is increasingly important to analyze its spatial distribution and seasonal and inter-annual variation its.

2.3. Auxiliary Data

To analyze the potential influencing factors of the main stream of the Yangtze River more effectively, we obtained the monthly sediment runoff data of Yichang, Hankou and Datong monitoring stations on the main stream of the Yangtze River from 2016 to 2020 from the website of Changjiang Water Conservancy Commission (http://www.ctg.com.cn/sxjt/sqqk/index.html; accessed on 26 January 2021). Yichang, Hankou, and Datong stations provided the sediment runoff data of the upper, middle, and lower reaches of the Yangtze River, respectively. Daily precipitation data from seven meteorological stations in Chongqing, Yibin, Anqing, Nanjing, Wuhan, Yichang, and Shanghai from 2016 to 2020 were acquired from the National Oceanic and Atmospheric Administration website (https://gis.ncdc.noaa.gov/maps/ncei/cdo/daily; accessed on 8 January 2021). The stations at Chongqing, Yibin, and Yichang; Wuhan; Anqing, Nanjing; and Shanghai provided the precipitation data for the upper, middle, and lower reaches of the Yangtze River, respectively. Daily water level data from 29 stations were obtained from the Theis website (http://hydroweb.theia-land.fr/; accessed on 1 February 2021) 2016 to 2020.

3. Method

3.1. Calculated SDD Based on GEE

It is challenging to analyze the spatio-temporal variation of water quality in a large area, especially for long time series. Excessive time is spent in data screening, data download, data pre-processing, and so on. Therefore, it is necessary to establish an efficient remote-sensing cloud data-processing platform. GEE is a free remote sensing cloud platform that specializes in processing satellite images and earth observation data. Although the GEE platform has synchronized surface reflectance data since 2017, these data have only been synchronized in the present study area since 2019. The spatial resolution of all bands of the Sentinel-2 surface reflectance data, called GEE, was 10 m. First, the Sentinel-2 data with cloud cover ≤ 40 were selected. Secondly, the Yangtze River water was extracted by utilizing multi-band water index (MBWI), Gongpeng 10 m global classification products, and K-means cluster analysis. Finally, FUI and hue angle α were calculated based on the water extraction results, and the results were retrieved based on the FUI and hue angle α of the Yangtze River. In addition, from 2017 to 2018, the Yangtze River SDD results were obtained by downloading Sentinel-2 L1C TOA data from the official ESA website, and atmospheric correction and band resampling were performed on the Sentinel-2 L1C TOA locally. The surface reflectance data with a spatial resolution of 10 m were obtained to retrieve the SDD results for the Yangtze River.

3.2. Waterbody Extraction

The Yangtze River Basin flows through 11 provinces, and there are many tributaries and surface features around the main stream of the Yangtze River. To avoid the water areas and surface features that were not in the study area being mistakenly extracted as water bodies, the global surface coverage map with a spatial resolution of 10 m produced by Gongpeng in 2019 based on Sentinel-2 remote sensing images and GEE was utilized for extraction [44]. Because the range of the water body is affected by external factors and changes at any time, the Gongpeng product was taken as the reference for the final water body extraction. Wang et al. analyzed the reflectance differences of seven types of ground objects, including water, vegetation, farmland, shadow, dark building area, bright building area and soil, in six bands, including the blue, green, red, near-infrared bands, and two short-wave infrared bands. Based on Landsat 8 OLI images, a new water index MBWI was proposed [45]:

$$\text{MBWI} = 2\text{Green-Red-NIR-SWIR1-SWIR2} \quad (1)$$

This index effectively inhibits the interference factors around the water body.

Water extraction based on the water index was used to distinguish between water and non-water portions of each remote sensing image by calculating the optimal threshold or employing an artificially selected experience threshold. This approach was mainly used

to calculate the optimal threshold of each remote sensing image based on the artificially selected experience value by utilizing iterative and statistical methods. To reduce the workload of calculating the optimal threshold and the human error caused by the artificial selection of an empirical threshold, we used MBWI gray images as input data, and then employed K-means clustering analysis to distinguish the water and non-water portions of the study area [46].

The accuracy evaluation of water extraction is based on the results of MNDWI processor in SNAP software. The result in this study is based on the same scene Sentinel-2 image, MRE = 1.04%. Figure 2 is the result of water extraction.

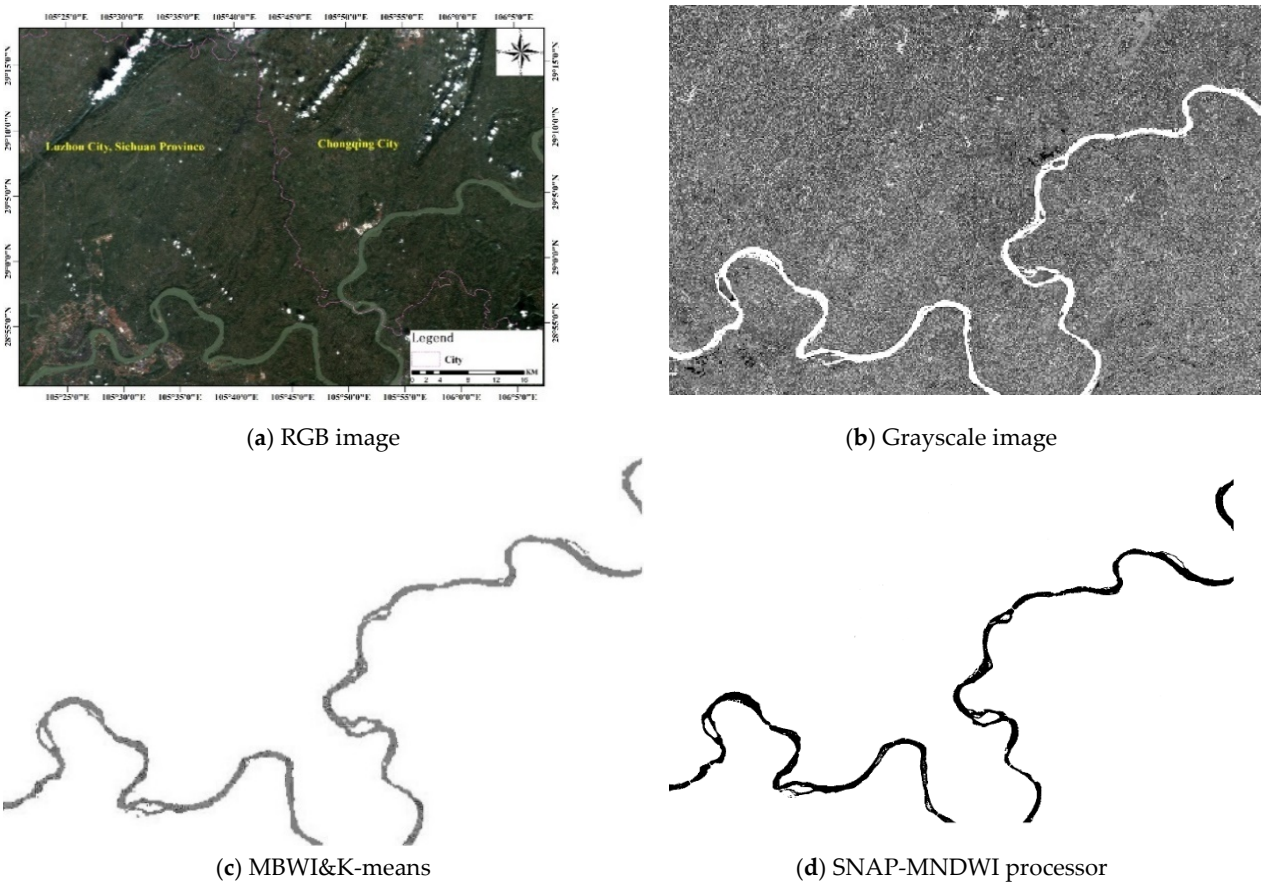

(**a**) RGB image (**b**) Grayscale image

(**c**) MBWI&K-means (**d**) SNAP-MNDWI processor

Figure 2. Result of waterbody extraction from Yangtze River: (**a**) RGB image; (**b**) Grayscale image; (**c**) MBWI&K-means; (**d**) SNAP-MNDWI processor.

3.3. SDD Calculation

Based on the Sentinel-2 images, hue angle α and FUI were calculated in five visible light bands: R (Coastal aerosol), R (Blue), R (Green), R (Red), and R (Vegetation Red Edge). The Commission International de l'é claim (CIE) is a standard chromaticity coordinate system [47]. Hue angle α is a parameter describing color in CIE color space. According to the color matching functions (CMFs), the weights of the X, Y, and Z tristimulus values are obtained:

$$\begin{cases} X = 11.756R(443) + 6.423R(490) + 53.696R(560) + 32.028R(665) + 0.529R(705) \\ Y = 1.744R(443) + 22.289R(490) + 65.702R(560) + 16.808R(665) + 0.192R(705) \\ Z = 62.696R(443) + 31.101R(490) + 1.778R(560) + 0.015R(665) + 0.000R(705) \end{cases} \quad (2)$$

The spatial resolution of the five abovementioned visible light bands is not consistent: that of R (443) is 60 m; that of R (490), R (560.0), R (665) is 10 m; and that of R (705) is 20 m. Therefore, before calculating the hue angle α, the spatial resolution of the five visible light bands of the local data has been unified as 10 m. R (443), R (490), R (560), R (665), and

R (705) in the formula correspond to R (443.9), R (496.6), R (560.0), R (664.5), and R (703.9) in the Sentinel-2 image, respectively.

The chromaticity coordinates in the CIE color space were calculated based on the three stimulus values of X, Y, and Z, and the calculated chromaticity coordinates are normalized to the range 0–1. Based on the chromaticity coordinate system, a new coordinate system was obtained:

$$\begin{cases} x = \frac{X}{X+Y+Z} \\ y = \frac{Y}{X+Y+Z} \end{cases} \quad (3)$$

Finally, the formula of hue angle α was obtained:

$$\alpha = \arctan\left(\frac{y - y_w}{x - x_w}\right) \times \frac{180}{\pi} + 180 \quad (4)$$

where y_w and x_w are (1/3, 1/3).

By correcting each hue angle α, the optimal linear relationship between the hue angle α based on hyperspectral calculation and the hue angle α calculated by satellite sensor was determined. Specifically, the hue angle α was corrected by compensating for the linear interpolation between the natural water spectrum and the sensor band [47]. Owing to the sensor band limitation, a large offset was produced, and the offset was not generated randomly. The calibration formula of hue angle α based on the Sentinel-2 sensor is as follows:

$$\Delta = 46.2094a^5 - 412.2561a^4 + 1385.5708a^3 - 2128.364a^2 + 1443.7115a - 341.6433 \quad (5)$$

where a is hue angle α divided by 100. By correcting the hue angle α, the hue angle α closer to the water color can be obtained. In this study, the definition of hue angle α was based on the point of equal-energy white light and increased with the main wavelength of color [47]. Note that the definition of hue angle α in this study is different from Hendrik Jan van der Woerd and Marcel Robert Wernand [48]. Based on the calculation of FUI and hue angle α, the SDD model is as follows [6]:

$$\begin{cases} FUI < 8, SDD = 3415.63 \times \alpha^{-1.49} \\ FUI \geq 8, SDD = 284.70 \times FUI^{-2.67} \end{cases} \quad (6)$$

3.4. Time and Spatial Aggregation

In this paper, the L1C TOA data of Sentinel-2 from 2017 to 2018 were downloaded from the ESA official website, and the surface reflectance data from GEE of Sentinel-2 from 2019 to 2020 were used to calculate the spatial distribution, seasonal variations, and inter-annual variations of the main stream of the Yangtze River (from Yibin City, Sichuan Province to the estuary) from 2017 to 2020 by quoting the retrieval model proposed by Wang et al. [6]. Generally, the 12 months in a year are divided into four seasons, where March–May is spring, June–August is summer, September–November is autumn, and December–February is winter. Because winter is from December to February every year, the seasonal and interannual variations were analyzed in this study by adding the results of the main stream of the Yangtze River in December 2016. However, there were no available data for the upper reaches of the Yangtze River from January to March 2018.

According to the 48 months from January to December in each year from 2017 to 2020 in the Yangtze River Basin, the spatial distribution characteristics and seasonal and interannual variations in the SDD of the Yangtze River were analyzed based on the remote sensing inversion results of the Sentinel-2A/2B remote sensing image. Because the results of single-day remote sensing image retrieval will be random, the monthly mean value could more accurately reflect the variations in the Yangtze River SDD in the statistical analysis. If multiple effective remote sensing images could be obtained in a month, the results of these images were calculated respectively, and the average of all the results of these images was taken to be the monthly average SDD for the relevant month. If only

one effective remote sensing image was available in a month, the SDD calculated from this remote sensing image was taken as the monthly average value of the corresponding month. The statistical process of obtaining annual average SDD involved reducing the random error of single day image statistics. The monthly average statistical data were taken as the basic unit of the interannual variations data. The monthly average over a year was taken as the annual average, and the average of the annual mean value obtained from 2017 to 2020 was taken as the four-year spatial distribution result of the Yangtze River. Table 1 shows the statistical results of valid images obtained in each month from 2017 to 2020.

Table 1. Image selection schedule.

Month	2016	2017	2018	2019	2020
January		32	93	101	105
February		69	160	52	158
March		35	196	163	201
April		106	258	207	192
May		67	108	180	231
June		47	240	180	106
July		160	330	229	71
August		162	389	384	267
September		73	248	273	171
October		120	303	194	184
November		159	205	163	206
December	87	180	71	195	139
Total	87	1210	2601	2321	2031

3.5. Accuracy Evaluation of SDD

In this study, the average relative error, root mean square error, and rate of change were used as the accuracy evaluation indices:

$$MRE = \frac{1}{n}\frac{|A - A'|}{A} \tag{7}$$

$$RMSE = \sqrt{\frac{\sum_1^n (A - A')^2}{n}} \tag{8}$$

$$Variation\ Rate = \frac{Standard\ deviation}{Mean\ value} \tag{9}$$

where A is the result of the calculation based on MODIS data, A' is the result of the calculation based on Sentinel-2 data, and n is the number of sampling points.

3.6. Model Adaptability

Because the main stream of the Yangtze River flows through Sichuan Province, Chongqing City, Hubei Province, Hunan Province, Jiangxi Province, Anhui Province, Jiangsu Province, and Shanghai City, the entire Yangtze River has a large span and the optical characteristics of the inland water are complex. Empirical algorithms based on the single-band model, band ratio, and band combination models cannot be adequately applied in different regions and seasons. Because the color of the water body is not affected by time and space, the quality of the water can be analyzed based on its color. Water color can be used to evaluate the degree of water clarity [48]. Moreover, there is a strong correlation between water color and water clarity in a wide range of inland and ocean waters [48]. Although water color is affected by different components in water, the correlation between water color and water quality is not affected by the change of water components [6]. In addition, Wang et al. compared the calculation model based on FUI and hue angle α with the band ratio, single band, and band combination model and concluded that the accuracy of the FUI and hue angle α calculation model was better than those of the empirical algorithms [6]. For a large range of inland water with many types of water, it is

difficult to achieve accurate atmospheric correction at present, and the FUI and hue angle α calculation results are less affected by the observation and atmospheric interference [48].

4. Result

4.1. SDD Results

Owing to the lack of in situ SDD data of Yangtze River and to prove that the SDD retrieval model proposed by Wang et al. has good universality and stability, in this study, the model was used to retrieve the water body characteristics of Baiyangdian Lake on 23 May 2019, and the accuracy evaluated with the in situ data of SDD on 21–22 May 2020. Figure 3 shows the SDD precision evaluation results, where R^2 = 0.7994, RMSE = 0.25 m, MRE = 23.7%, and Pearson correlation coefficient = 0.89, which proves that the model has good universality and stability.

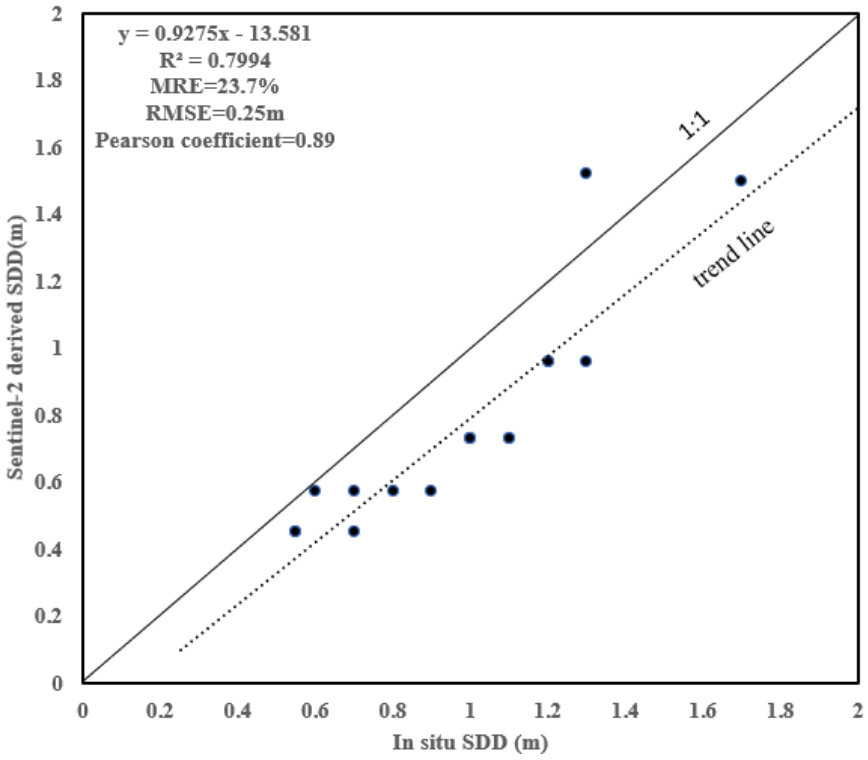

Figure 3. Scatterplots showing the derivation of the accuracies of Sentinel-2 derived SDD in comparison with in situ SDD.

To further prove that the model proposed by Wang et al. can be adequately applied to Sentinel-2 data, in this study, we acquired images for the central area of the Three Gorges Reservoir in the upper reaches of the Yangtze River, on 13 October 2020 and 14 April 2020; for the middle reaches of Wuhan City and Huanggang City, Hubei Province, on 11 October 2020; and for the downstream Nantong City and Taizhou City, Jiangsu Province, on 18 February 2020 and 5 September 2020. Consequently, if the variation rate of SDD estimated by the two data sources was less than 15%, then the results could be considered reliable. Figure 4 shows the sample point location. Two factors were considered when selecting the sample points. First, if the sample points were selected on the shore, there could be affected due to optical shallow water or pollutants. Second, the spatial resolution of the MODIS and Sentinel-2 remote sensing image data were 500 and 10 m, respectively. Hence, if a sample was selected on the shore, it could also be affected by mixed pixels. It was necessary to avoid the effects of these interference factors when selecting the points. To achieve this objective, the distance between each selected sample points and the shore was required to be greater than 1 km.

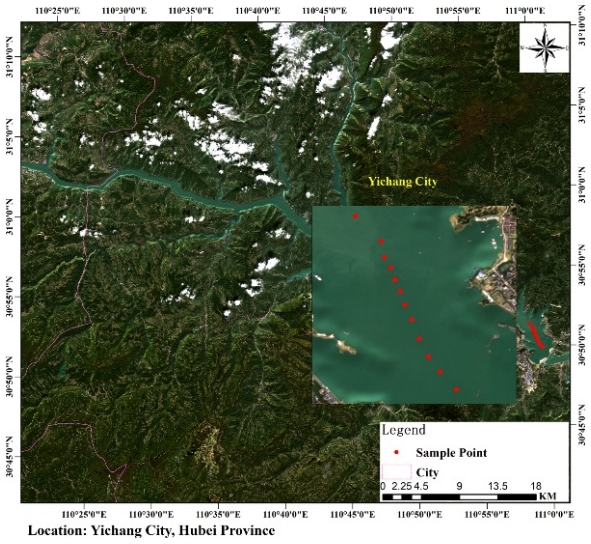

(**a**) Three Gorges Reservoir.

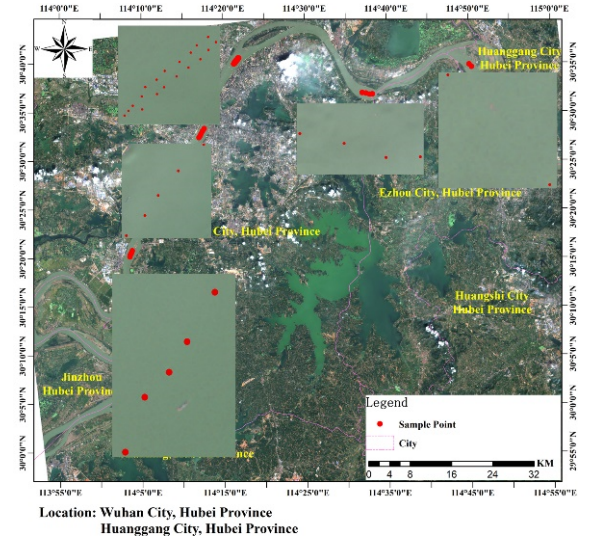

(**b**) Wuhan City and Huanggang City, Hubei Province.

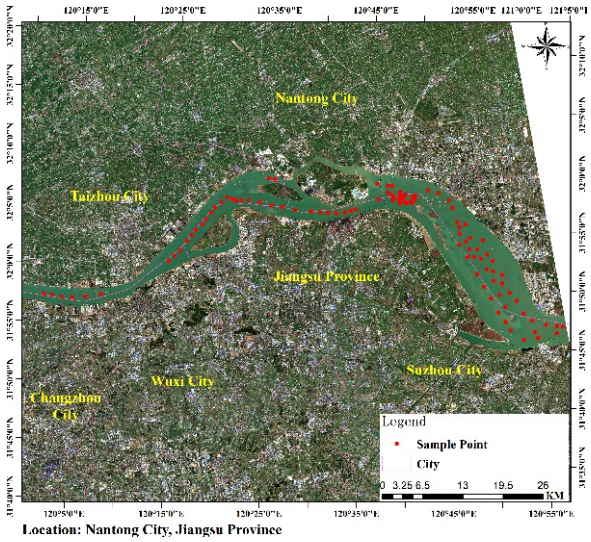

(**c**) Nantong City and Taizhou City, Jiangsu Province.

Figure 4. Sample Point: (**a**) Three Gorges Reservoir; (**b**) Wuhan City and Huanggang City, Hubei Province; (**c**) Nantong City and Taizhou City, Jiangsu Province.

In MODIS remote sensing image data, taking each sample point as the center, 3 × 3 pixels are selected to calculate the mean value, standard deviation, and variation rate of the region, and the average variation rate is 11.7%. The spatial resolution of the MODIS remote sensing images is 500 m, 3 × 3 pixels, i.e., 1.5 × 1.5 km. Hence, to ensure that the selected areas of the Sentinel-2 remote sensing images, 150 × 150 pixels were selected in Sentinel-2 image with each sample point as the center. Again, the mean value, standard deviation, and average variation rate of each region were also calculated 11.6%. Figure 5 presents the SDD precision evaluation results, where R^2 = 0.8852, RMSE = 0.06m, MRE = 11.4%, Pearson correlation coefficient = 0.94.

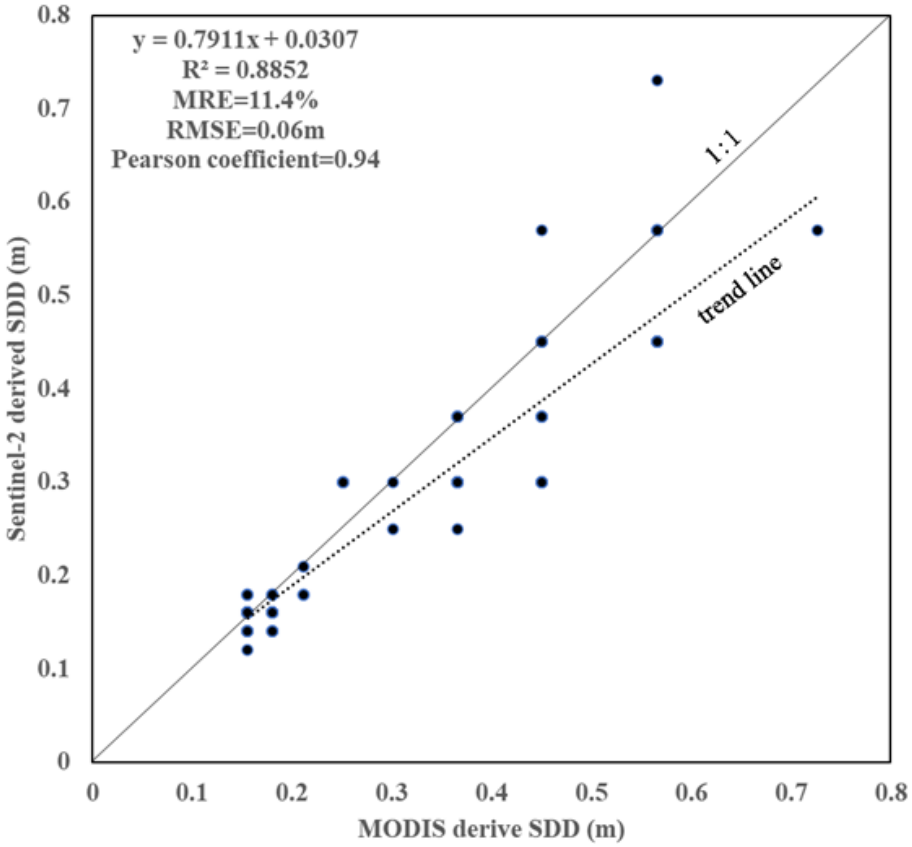

Figure 5. Scatterplots showing the derivation of accuracies of MODIS derived SDD in comparison with Sentinel-2 derived SDD.

4.2. Spatial Distribution

Figure 6 shows the calculated the spatial distribution of the SDD in the main stream of the Yangtze River from January to December in 2017–2020. Additionally, Figure 6 shows the mean value of the SDD from 2017 to 2020. The spatial distribution pattern of the SDD in the main stream of the Yangtze River is high in the west and low in the east, with the highest water clarity in the upper reaches and the lowest in the lower reaches. The mean value of SDD in the main stream of the Yangtze River is 0.58 m, and the mean value of SDD of the upper, middle, and lower streams are 0.96, 0.49, and 0.29 m, respectively. The upper reaches of the Yangtze River are from Yibin City, Sichuan Province to Yichang City, Hubei Province. The SDD in the upper reaches is higher on the east and west sides and lower in the middle. Specifically, it is more than 1 m on the west and east sides. The middle reaches of the Yangtze River are from Yichang City, Hubei Province to Hukou County, Jiujiang City, Jiangxi Province. The SDD in the middle reaches is high in the west and low in the east. Taking Dongting Lake in Hunan Province as the boundary, the SDD on the west side of the Dongting Lake is higher than that on the east side. The lower reaches of the Yangtze River are from Hukou County, Jiujiang City, Jiangxi Province to the estuary of the Yangtze

River. According to the spatial distribution of the SDD in the main stream of the Yangtze River, the upper reaches are better than the middle reaches, and the middle reaches are better than the lower reaches.

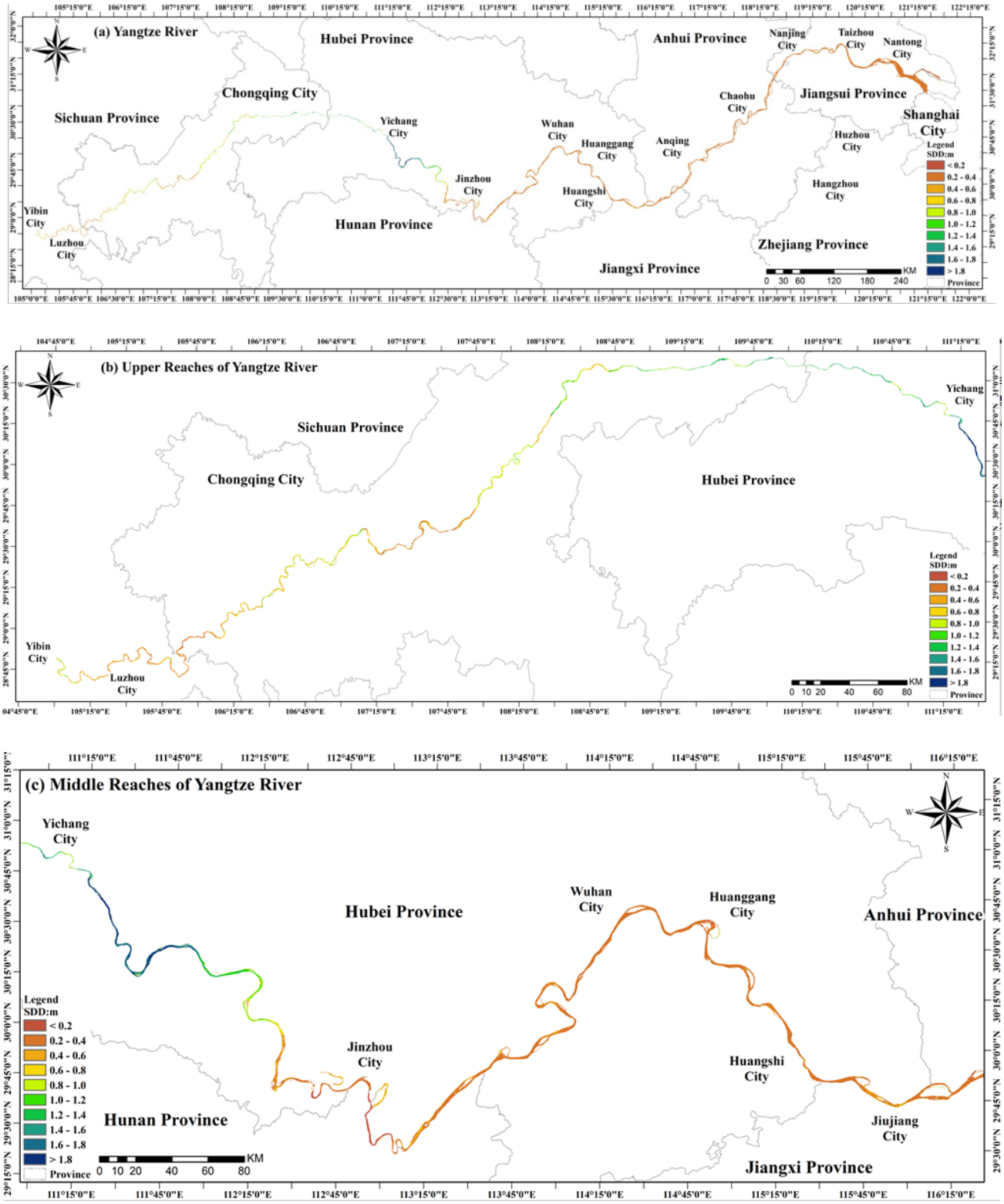

Figure 6. *Cont.*

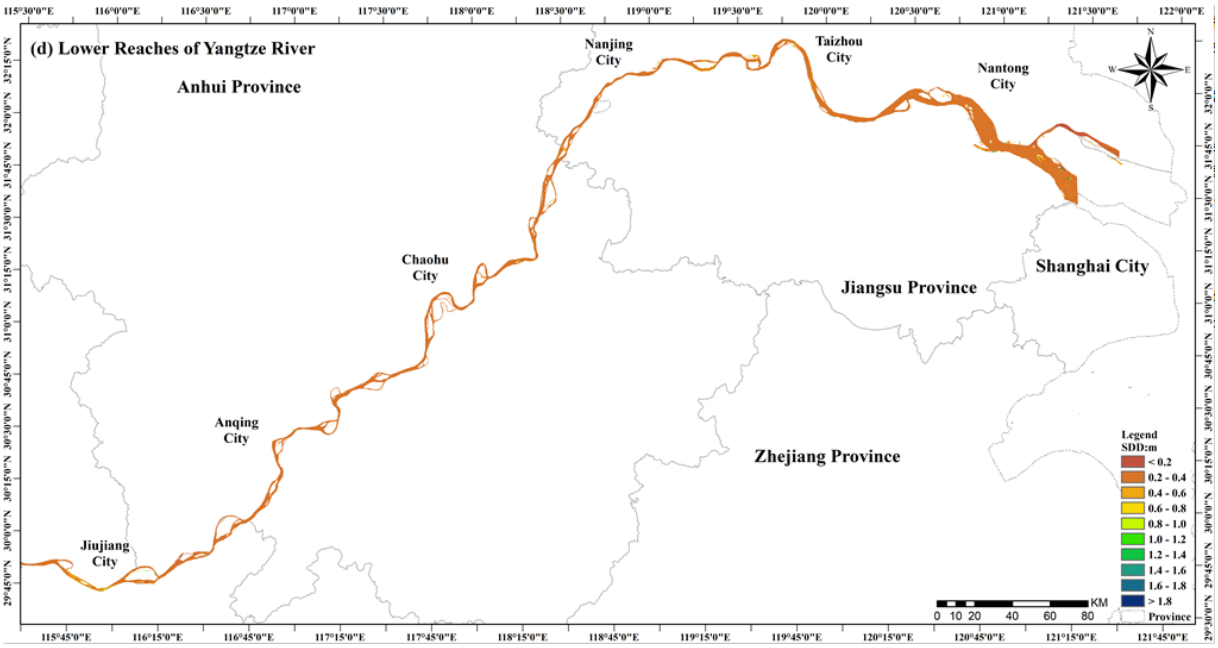

Figure 6. Spatial distribution of SDD in 2017–2020; (**a**) Yangtze River full view; (**b**) upper reaches; (**c**) middle reaches; (**d**) lower reaches of Yangtze River.

4.3. Seasonal Variation

Figure 7 depicts the seasonal variation of SDD in the main stream of the Yangtze River from 2017 to 2020. The seasonal variation range of SDD in the upper reaches of the Yangtze River is large at 1.39, 1.11, 0.26, and 0.87 m in winter, spring, summer, and autumn, respectively. The monthly mean value of the upper reaches is the lowest in June and highest in December. In the middle reaches of the Yangtze River, the mean value of SDD is 0.61, 0.57, 0.35, and 0.46 m in winter, spring, summer, and autumn. The monthly mean value of SDD in the middle reaches of the Yangtze River is the lowest in July and the highest in February. The SDD in the lower reaches of the Yangtze River is higher in winter and spring with the mean value of 0.31 and 0.33 m, respectively, and lower in summer and autumn, with the mean value of 0.28 and 0.27 m, respectively. The monthly mean value of SDD in the lower reaches of the Yangtze River is the highest in February and the lowest in August. The upper, middle, and lower reaches of the Yangtze River are higher in winter and spring and lower in summer and autumn. The maximum and minimum of the monthly mean value of SDD appeared in winter and summer, respectively. The overall seasonal variation of SDD in the main stream of the Yangtze River is similar to that in the upper stream. The mean value of SDD is 0.77, 0.67, 0.29, and 0.53 m in winter, spring, summer, and autumn, respectively. The monthly mean value of the main stream of the Yangtze River is the lowest in July and the highest in December. In addition, the seasonal variation trend of the SDD in Yangtze River is very similar to that in the Upper Yangtze River.

4.4. Inter-Annual Variation

Figure 8 shows the inter-annual variations of the SDD in Yangtze River from 2017 to 2020. Table 2 summarizes the annual mean value of SDD in the upper, middle, and lower reaches of the Yangtze River as well as the main stream from 2017 to 2020. Generally, the annual variation range of the SDD in the main stream of the Yangtze River from 2017 to 2020 was large. The mean value of the main stream of the Yangtze River was the largest in winter 2017 and the smallest in summer 2020, at 0.96 and 0.24 m, respectively. Simultaneously, the four seasonal and annual mean value of SDD the upper, middle, and lower reaches of the Yangtze River as well as the main stream were calculated, respectively. The inter-annual

variations of the SDD in upper reaches of the Yangtze River and the main stream were basically the same, showing a downward trend from winter to summer every year and upward trend in autumn. In 2017–2020, the annual mean value of SDD was the largest in winter and the smallest in summer. However, in 2018, the mean value in the upper reaches of the Yangtze River in autumn was slightly higher than that in winter. The inter-annual variations of the SDD in the middle and lower reaches of the Yangtze River were similar but slightly different from that in the upper and main reaches of the Yangtze River overall. In the middle and lower reaches of the main stream of the Yangtze River, in 2017 and 2019, the mean value of SDD in winter was the largest, and in 2018 and 2020, the mean value of SDD in spring was the largest. In the middle reaches of the main stream of the Yangtze River, the annual mean value of SDD in summer 2018–2020 was small, and only in spring 2017 was it the minimum. In the lower reaches of the main stream of the Yangtze River, the mean value of SDD was the smallest in autumn 2018 and 2019, whereas the mean value of SDD was the smallest in spring and summer in 2017 and 2019, respectively. The maximum and minimum annual mean value of SDD in the upper, middle, and lower reaches and main stream of the Yangtze River were 1.2 and 0.79, 0.76 and 0.35, 0.35 and 0.25, and 0.77 and 0.47 m, respectively.

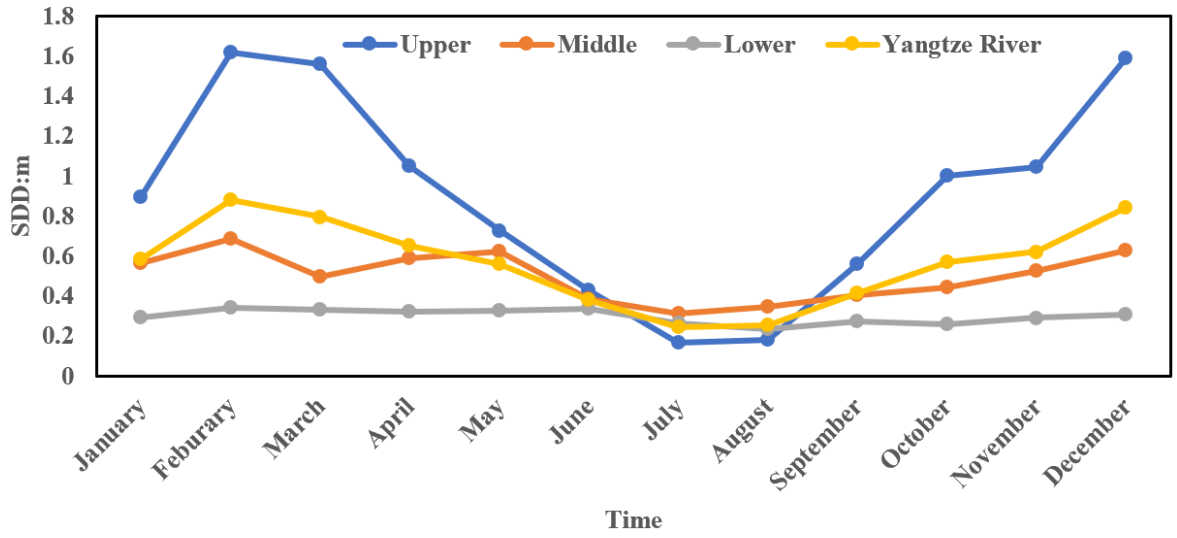

Figure 7. The results of seasonal variation of upper reaches, middle reaches, and lower reaches of Yangtze River.

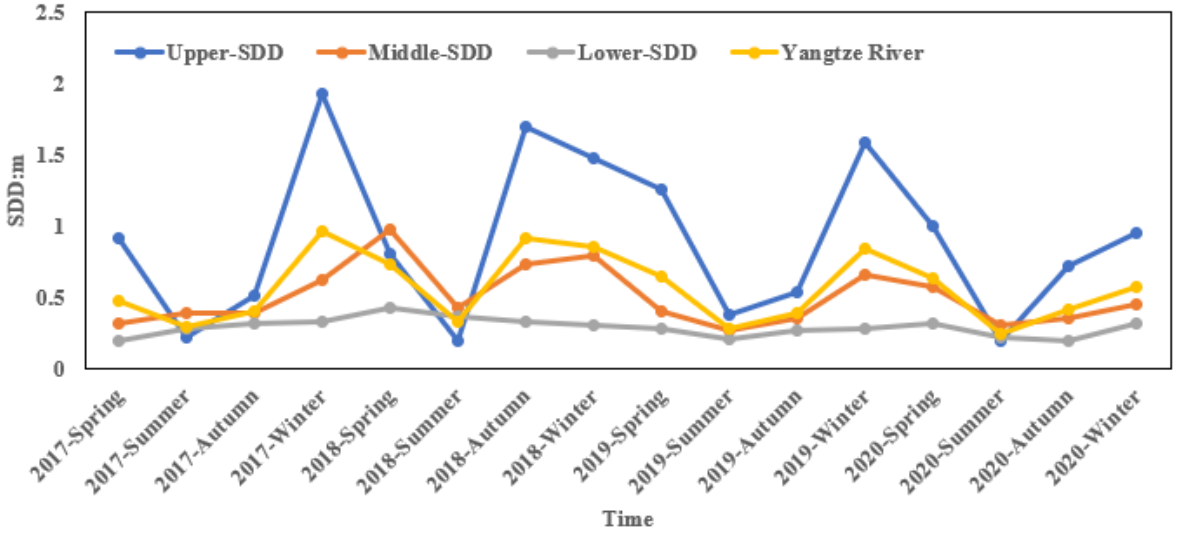

Figure 8. The results of inter-annual variation of upper reaches, middle reaches, and lower reaches of the Yangtze River.

Table 2. The annual mean value results of upper reaches, middle reaches, lower reaches of the Yangtze River SDD.

Year	Upper Reaches (m)	Middle Reaches (m)	Lower Reaches (m)	Yangtze River (m)
2017	0.91	0.43	0.29	0.55
2018	1.2	0.76	0.35	0.77
2019	0.79	0.35	0.25	0.47
2020	0.82	0.43	0.26	0.51

5. Discussion

5.1. Driving Forces of Water Clarity

The correlation coefficient is typically used to express the correlation between two variables. When one variable is increasing or decreasing, the other is increasing or decreasing, and the two variables are positively correlated. When one variable increase or decreases, while the other decreases or increases, the two variables are negatively correlated. The larger the correlation coefficient is, the stronger is the correlation degree. The smaller the correlation coefficient is, the smaller is the correlation degree.

There are three commonly used correlation coefficients: the Pearson correlation coefficient, Spearman correlation coefficient, and Kendall correlation coefficient. In this study, the Pearson correlation coefficient was used to describe the correlation of two variables:

$$\rho_{X,Y} = \frac{\mathrm{cov}(X,Y)}{\sigma_X \sigma_Y} = \frac{\sum XY - \frac{\sum X \sum Y}{N}}{\sqrt{\left(\sum X^2 - \frac{(\sum X)^2}{N}\right)\left(\sum Y^2 - \frac{(\sum Y)^2}{N}\right)}} \quad (10)$$

There is a certain degree of similarity in the variations of water quality in inland, coastal and ocean water, and they all showed a downward trend [26]. In different areas of water, the factors that affect the water quality vary [4,5,49,50]. In the main stream area of the Yangtze River, sediment runoff, precipitation, and water level may be the main factors leading to changes in water clarity. The correlations between pairs of the factors of sediment runoff, precipitation, and water level are all positive, as shown in Figure 9. The correlation coefficients of sediment runoff and precipitation, sediment runoff and water level, precipitation and water level were 0.66, 0.64, and 0.31, respectively. Due to the rise of water level in the main stream of the Yangtze River caused by precipitation, the increase in surface runoff introduced a large volume of sediment, leading to an increase in sediment runoff.

Figure 10 presents the relationships between the three driving factors of sediment runoff, water level, and precipitation in the upper reaches of the Yangtze River. There are negative correlations between the SDD and runoff, SDD and water level, and SDD and PRCP, which have correlation coefficients of -0.79, -0.62 and -0.75, respectively. During 2017–2020, the upper reaches of the Yangtze River have the lowest in summer; higher in spring, autumn, and winter than in summer, and the highest in winter, but slightly higher in spring than in winter 2020. The main reason for the rainfall being the lowest in summer is that the rainy season is from May to September every year, and the flood season of the Yangtze River is from July to August or September every year. Although the precipitation along the Yangtze River increases in summer, the temperature of the Qinghai Tibet Plateau in the upper reaches of the Yangtze River Basin is increasing significantly under the background of global warming due to atmospheric greenhouse effect caused by human activities. The head temperature shows an increasing trend, and the melting rate of ice and snow is accelerating [50]. The increase in surface runoff introduces a large volume of sediment, which may increase water turbidity and cause the water quality to decrease in summer. The amount of sediment runoff, water level, and precipitation in summer 2020 are significantly higher than those in summer 2017–2019, which may have been due to the increase in rainfall in the upstream area caused probably by the Hongfeng typhoon in

summer 2020, which brought a large amount of precipitation and caused water pollution. The increase in water level and sediment runoff led to a decreased SDD.

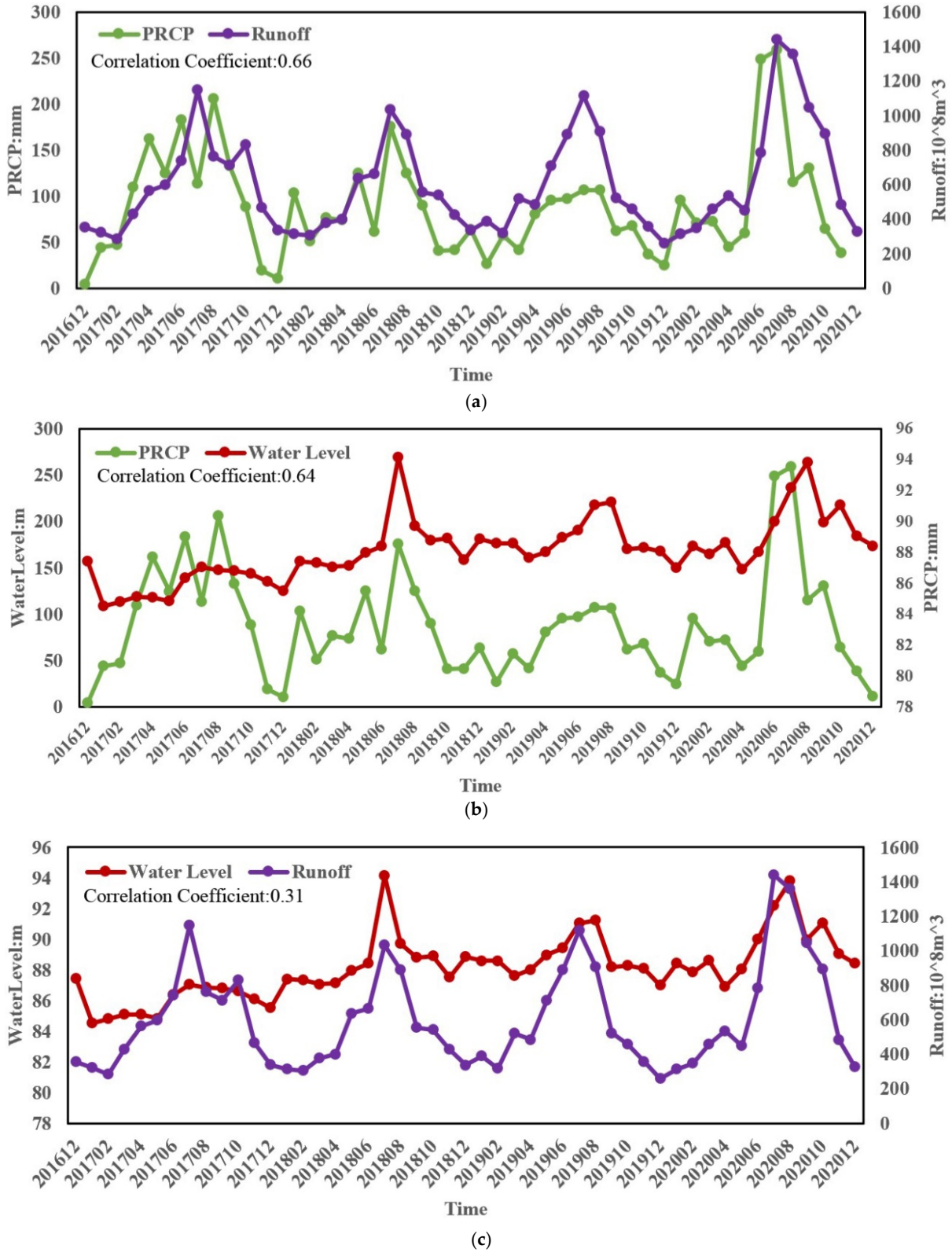

Figure 9. The relationship between runoff, water level, PRCP; (**a**) the relationship between PRCP and water level; (**b**) the relationship between PRCP and water level; (**c**) the relationship between runoff and water level.

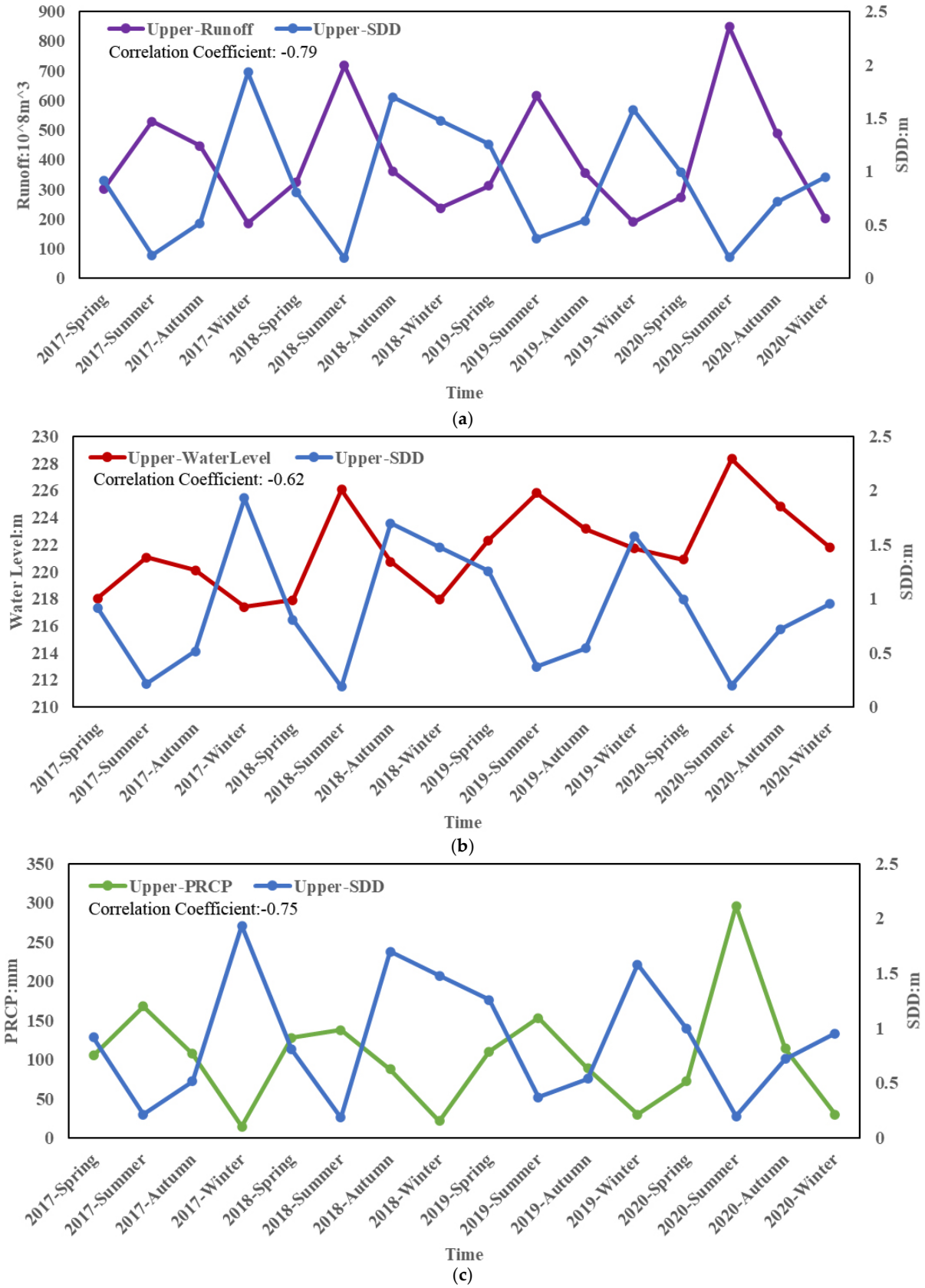

Figure 10. The relationship between the upper reaches of the Yangtze River and runoff, water level, PRCP; (**a**) the relationship between the SDD and runoff; (**b**) the relationship between the SDD and water level; (**c**) the relationship between the SDD and PRCP.

Figures 11 and 12 show the relationships between the sediment runoff, water level, and precipitation, in the middle and lower reaches of the Yangtze River. The middle reaches of the Yangtze River are negatively correlated with sediment runoff and precipitation, whereas the middle reaches of the Yangtze River are negatively correlated with the water level. The correlation coefficients between the SDD and sediment runoff, SDD and water level, and SDD and PRCP were calculated to be −0.62, 0.18, and −0.46, respectively. The lower reaches of the Yangtze River are negatively correlated with sediment runoff and precipitation, and the correlation coefficients between the SDD and sediment runoff, SDD and water level, and SDD and PRCP were calculated to be −0.47, −0.49, and −0.22. The correlations of the middle and lower reaches are not stronger than those of the upper reaches. There may be two main reasons for this finding. First, the large-scale construction of reservoirs in the Yangtze River basin may decrease sediment runoff. According to statistics, approximately 22% of the sediment in global rivers is intercepted in reservoirs every year [51]. For example, the implementation of the Three Gorges Project and the South to North Water Diversion Project has changed the general law of the distribution of water resources in the Yangtze River [52]. Since the Three Gorges Reservoir began operation in 2003, the sediment runoff in the middle and lower reaches of the Yangtze River has decreased significantly [36]. Since the 1950s, more than 350,000 dams have been built in the Yangtze River Basin. By 2015, more than 280 large reservoirs and 130 medium-sized reservoirs have been built in the Yangtze River Basin, with a total capacity of more than 360 billion m^3. These reservoirs significant affect the annual distribution of sediment runoff through peak shaving and dry compensation, resulting in a significant increase in sediment runoff in the middle and lower reaches of the Yangtze River during the dry season, a decrease in sediment runoff in the wet season [36]. Simultaneously, after the impoundment and operation of the reservoir, a large amount of sediment is intercepted in the reservoir, significantly decreasing in the sediment runoff of the main stream of the Yangtze River, especially in the middle and lower reaches [53]. Meanwhile, pollution, such as urban sewage, garbage pollution, and chemical pollution, in the middle and lower reaches of the main stream of the Yangtze River may be more serious.

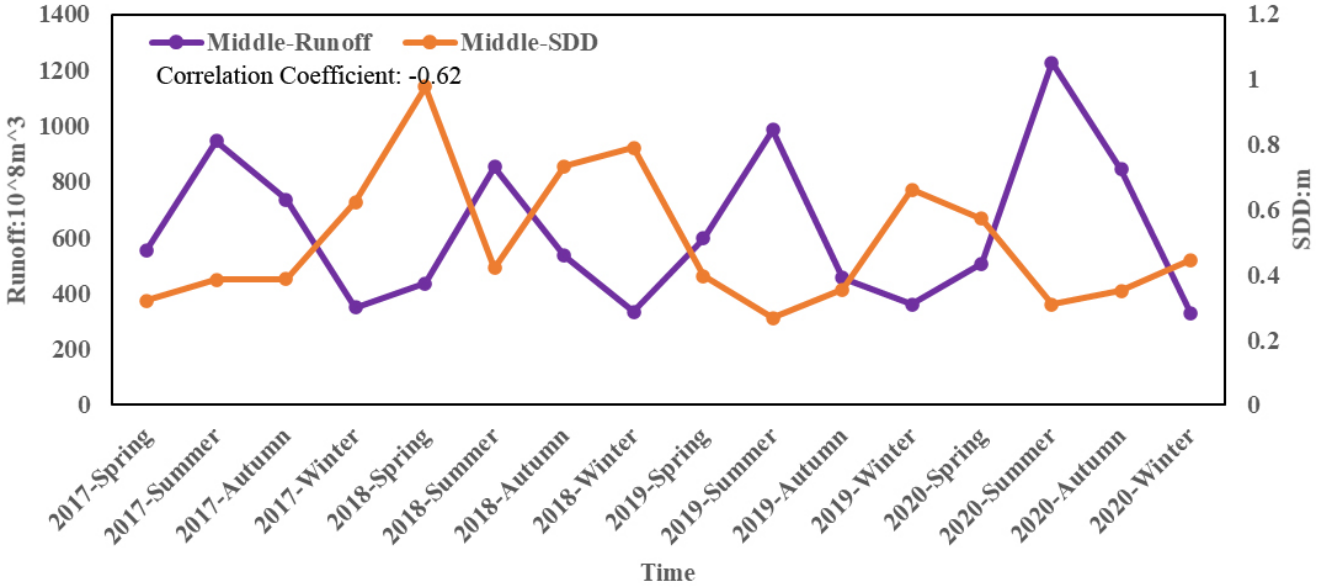

(**a**)

Figure 11. *Cont.*

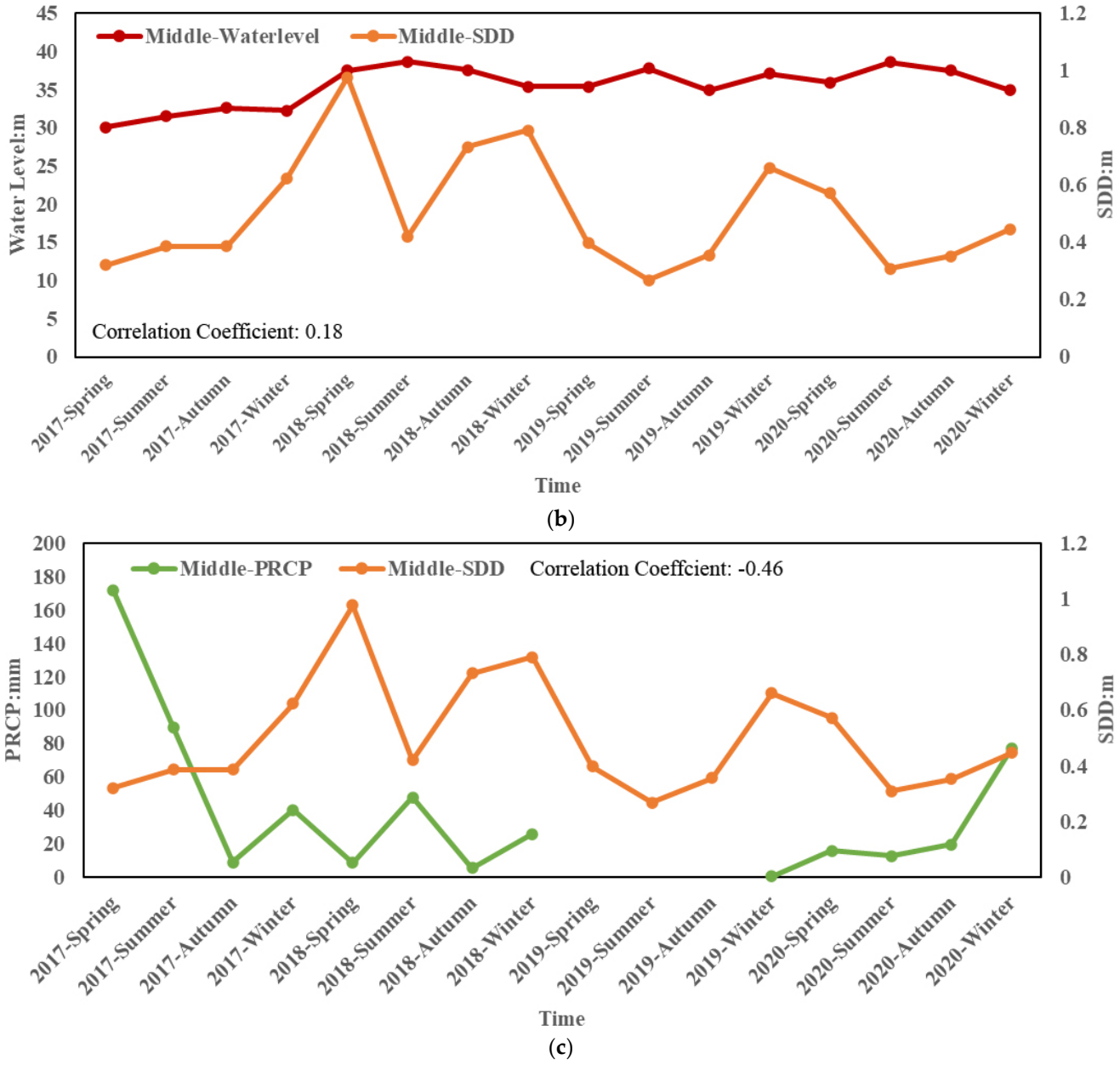

Figure 11. The relationship between the middle reaches of the Yangtze River and runoff, water level, PRCP; (**a**) the relationship between the SDD and runoff; (**b**) the relationship between the SDD and water level; (**c**) the relationship between the SDD and PRCP.

5.2. Deficiencies

The study uses the SDD retrieval model proposed by Wang et al. [6], which is based on simulation, in situ, and MODIS matching data. However, the in situ dataset in this model does not include the in situ and Sentinel-2 matching data of the Yangtze River Basin, which may limit the results of the SDD retrieval of the Yangtze River. Noteworthily, SDD is negatively correlated with hue angle and FUI, which has a theoretical basis. Therefore, the relative size of the SDD of the Yangtze River obtained by Wang's model is unproblematic; that is, the spatial distribution and temporal change trend are not complicated. However, it should be noted that there may be some errors in the absolute value of the SDD results retrieved by Wang's model [6].

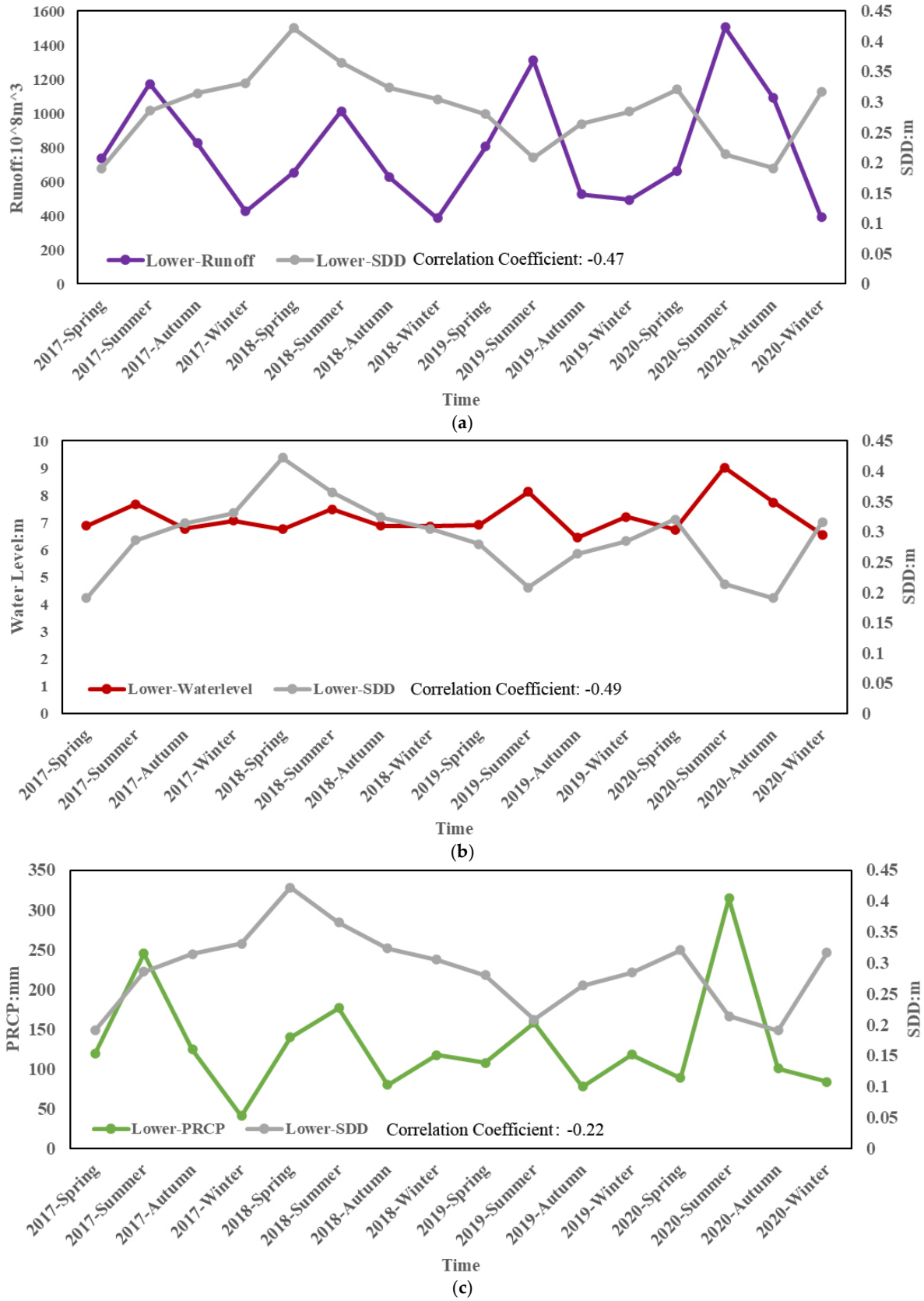

Figure 12. The relationship between the lower reaches of the Yangtze River and runoff, water level, PRCP; (**a**) the relationship between the SDD and runoff; (**b**) the relationship between the SDD and water level; (**c**) the relationship between the SDD and PRCP.

Most water quality parameters retrieval models that employ empirical methods are based on the original spectral characteristics of optical images. Niroumand–Jadidi et al. and Gholizadeh et al. provided a comprehensive discussion of the common retrieval methods to determine sensors suitable for selecting the optimal band combination and quantitatively evaluating 11 water quality parameters when constructing the water quality parameter retrieval model [54,55]. However, the retrieval models based on the spectral index are all oriented to some typical study areas. For the models to be applied to the Yangtze River region, it is generally necessary to optimize them based on the in situ SDD data of the Yangtze River. However, considering the lack of in situ SDD data, we used the SDD retrieval model, which has been verified to be suitable for various water bodies in China [6].

In the future, if more in situ SDD data from the Yangtze River are obtained, we will compare the models constructed by various spectral indices. In addition, we will construct the SDD retrieval model according to the spectral characteristics, evaluate its accuracy, and compare it with the existing SDD retrieval model.

6. Conclusions

Owing to the large span of the Yangtze River, the complexity and dynamic variability of the optical properties of inland water limit the applicability of empirical and analytical models. FUI and hue angle α are optical parameters that are not affected by changes in the water components and light field and have strong anti-interference abilities with regard to the atmosphere. The accuracy evaluation results of the model: R^2 = 0.8854, RMSE = 0.07m, MRE = 14.0%, Pearson correlation coefficient of 0.93, which proves that the model based on MODIS data can be well applied in Sentinel-2. Spatially, the upper reaches of the Yangtze River are generally higher than those of the lower and middle reaches, and lower reaches of the Yangtze River were the lowest. The upper reaches of the Yangtze River exhibited a larger time variation range than the middle and lower reaches. From 2017 to 2020, the upper and lower reaches of the Yangtze River and the overall SDD showed a weak downward trend, whereas the middle reaches of the Yangtze River almost unchanged. The results show that Sentinel-2 remote sensing image can retrieve the results of large-scale and long-time series. Monitoring water quality based on remote sensing technology is an economic, efficient, and intuitive monitoring method and can provide valuable reference information for the development of corresponding water quality management policies for the main stream of the Yangtze River.

Author Contributions: Conceptualization, Y.Z.; methodology, Y.Z. and S.W.; software, Y.Z.; validation, Q.S., F.Z. and S.W.; formal analysis, Y.Z.; investigation, Y.Z.; resources, J.L.; data curation, F.Z.; writing—original draft preparation, Y.Z.; writing—review and editing, J.L., S.W., Q.S. and F.Z.; visualization, F.Z.; supervision, F.Z.; project administration, F.Z.; funding acquisition, F.Z. All authors have read and agreed to the published version of the manuscript.

Funding: This work was supported by the Hainan Provincial Department of Science and Technology (ZDKJ2019006), the Science and Technology Service Network Initiative, Chinese Academy of Sciences (KFJ-STS-ZDTP-077), Open Research Fund of National Earth Observation Data Center (No.NODAOP2020017), the National Natural Science Foundation of China (41971318), and Dragon 5 Cooperation (No.59193).

Acknowledgments: The authors would like to thank ESA and GEE for providing the Sentinel-2 data.

Conflicts of Interest: The authors declare no conflict of interest.

References

1. The Yangtze River Water Conservancy Commission of the Ministry of Liberia. *Atlas of the Yangtze River Basin*; Map Publishing House: China, Beijing, 1999; pp. 239–240.
2. Aas, E.; Høkedal, J.; Sørensen, K. Secchi depth in the Oslofjord-Skagerrak area: Theory, experiments and relationships to other quantities. *Ocean Sci.* **2014**, *10*, 177–199. [CrossRef]
3. Carlson, R.E. A trophic state index for lakes. *Limnol. Oceanogr.* **1977**, *22*, 361–369. [CrossRef]

4. Olmanson, L.G.; Bauer, M.E.; Brezonik, P.L.A. A 20-Year Landsat water clarity census of Minnesota's 10,000 lakes. *Remote Sens. Environ.* **2008**, *112*, 4086–4097. [CrossRef]
5. Olmanson, L.G.; Brezonik, P.L.; Finlay, J.C.; Bauer, M.E. Comparison of Landsat 8 and Landsat 7 for regional measurements of CDOM and water clarity in lakes. *Remote Sens. Environ.* **2016**, *185*, 119–128. [CrossRef]
6. Wang, S.L.; Li, J.S.; Zhang, B.; Lee, Z.; Spyrakos, E.; Feng, L.; Liu, C.; Zhao, H.; Wu, Y.; Zhu, L.; et al. Changes of water clarity in large lakes and reservoirs across China observed from long-term MODIS. *Remote Sens. Environ.* **2020**, *247*, 111949. [CrossRef]
7. McCullough, I.M.; Loftin, C.S.; Sader, S.A. Combining lake and watershed characteristics with Landsat TM data for remote estimation of regional lake clarity. *Remote Sens. Environ.* **2012**, *123*, 109–115. [CrossRef]
8. Lee, Z.P.; Shang, S.L.; Du, K.P.; Wei, J.W. Resolving the long-standing puzzles about the observed Secchi depth relationships. *Limnol. Oceanogr.* **2018**, *63*, 2321–2336. [CrossRef]
9. Doron, M.; Babin, M.; Hembise, O.; Mangin, A.; Garnesson, P. Ocean transparency from space: Validation of algorithms estimating Secchi depth using MERIS, MODIS and SeaWiFs data. *Remote Sens. Environ.* **2011**, *115*, 2986–3001. [CrossRef]
10. Mouw, C.B.; Greb, S.; Aurin, D.; DiGiacomo, P.M.; Lee, Z.; Twardowski, M.; Binding, C.; Hu, C.; Ma, R.; Moore, T.; et al. Aquatic color radiometry remote sensing of coastal and inland waters: Challenges and recommendations for future satellite missions. *Remote Sens. Environ.* **2015**, *160*, 15–30. [CrossRef]
11. Chipman, J.W.; Lillesand, T.M.; Schmaltz, J.E.; Leale, J.E.; Nordheim, M.J. Mapping lake water clarity with Landsat images in Wisconsin, USA. *Can. J. Remote Sens.* **2004**, *30*. [CrossRef]
12. Nelson, S.A.C.; Soranno, P.A.; Cheruvelil, K.S.; Batzli, S.A.; Skole, D.L.L. Regional assessment of lake water clarity using satellite remote sensing. *J. Limnol.* **2003**, *62*, 27–32. [CrossRef]
13. Ren, J.L.; Zheng, Z.B.; Li, Y.M.; Lv, G.N.; Wang, Q.; Lyu, H.; Huang, C.C.; Liu, G.; Du, C.G.; Mu, M.; et al. Remote observation of water clarity patterns in Three Gorges Reservoir and Dongting Lake of China and their probable linkage to the Three Gorges Dam based on Landsat 8 imagery. *Sci. Total Environ.* **2018**, *625*, 1554–1566. [CrossRef] [PubMed]
14. Duan, H.T.; Ma, R.H.; Zhang, Y.L.; Zhang, B. Remote-sensing assessment of regional inland lake water clarity in Northeast China. *Limnology* **2009**, *10*, 135–141. [CrossRef]
15. Lathrop, R.G.; Lillesand, T.M. Use of thematic mapper data to assess water quality in Green Bay and central Lake Michigan. *Photogramm. Eng. Remote Sens.* **1986**, *52*, 671–680.
16. Lathrop, R.G. Landsat thematic mapper monitoring of turbid inland water quality. *Photogramm. Eng. Remote Sens.* **1992**, *58*, 465–470.
17. Giardino, C.; Pepe, M.; Brivio, P.A.; Ghezzi, P.; Zilioli, E. Detecting chlorophyll, Secchi disk depth and surface temperature in a sub-alpine lake using landsat imagery. *Sci. Total Environ.* **2001**, *268*, 19–29. [CrossRef]
18. Kloiber, S.M.; Brezonik, P.L.; Bauer, M.E. Application of Landsat imagery to regional-scale assessments of lake clarity. *Water Res.* **2002**, *36*, 4330–4340. [CrossRef]
19. Kloiber, S.M.; Brezonik, P.L.; Olmanson, L.G.; Bauer, M.E. A procedure for regional lake water clarity assessment using Landsat multispectral data. *Remote Sens. Environ.* **2002**, *82*, 38–47. [CrossRef]
20. Hellweger, F.L.; Schlosser, P.; Lall, U.; Weissel, J.K. Use of satellite imagery for water quality studies in New York Harbor. *Estuar. Coast. Shelf Sci.* **2004**, *61*, 437–448. [CrossRef]
21. Lee, Z.P.; Darecki, M.; Carder, K.L.; Davis, C.O.; Stramski, D.; Rhea, W.J. Diffuse attenuation coefficient of downwelling irradiance: An evaluation of remote sensing methods. *J. Geophys. Resour. Oceans* **2005**, *110*. [CrossRef]
22. Lee, Z.P.; Weidemann, A.; Kindle, J.; Arnone, R.; Carder, K.L.; Davis, C. Euphotic zone depth: Its derivation and implication to ocean-color remote sensing. *J. Geophys. Res.* **2007**, *112*, C03009. [CrossRef]
23. Binding, C.E.; Jerome, J.H.; Bukata, R.P.; Booty, W.G. Trends in water clarity of the lower great lakes from remotely sensed aquatic color. *J. Great Lakes Resour.* **2007**, *2*, 828–841. [CrossRef]
24. Budd, J.W.; Drummer, T.D.; Nalepa, T.F.; Fahnenstiel, G.L. Remote sensing of biotic effects: Zebra mussels (Dreissena polymorpha) influence on water clarity in Saginaw Bay, Lake Huron. *Limnol. Oceanogr.* **2001**, *46*, 213–223. [CrossRef]
25. Gower, J.F.R. SeaWiFS global composite images show significant features of Canadian waters for 1997–2201. *Can. J. Remote Sens.* **2004**, *30*, 26–35. [CrossRef]
26. Shi, K.; Zhang, Y.L.; Zhu, G.W.; Qin, B.; Pan, D.L. Deteriorating water clarity in shallow waters: Evidence from long term MODIS in-situ observations. *Int. J. Appl. Earth Obs. Geoinf.* **2018**, *68*, 287–297. [CrossRef]
27. Feng, L.; Hu, C.M.; Chen, X.L.; Song, Q.J. Influence of the Three Gorges Dam on total suspended matters in the Yangtze Estuary and its adjacent coastal waters: Observations from MODIS. *Remote Sens. Environ.* **2014**, *140*, 779–788. [CrossRef]
28. Shi, H.Y.; Gao, C.; Dong, C.M.; Xia, C.S.; Xu, G.L. Variations of river islands around a large city along the Yangtze River from satellite remote sensing images. *Sensors* **2017**, *17*, 2213. [CrossRef]
29. Wang, J.J.; Lu, X.X.; Liew, S.C.; Zhou, Y. Retrieval of suspended sediment concentrations in large turbid rivers using Landsat ETM+: An example from the Yangtze River, China. *Earth Surf. Process. Landf.* **2009**, *34*, 1082–1092. [CrossRef]
30. Hou, X.J.; Feng, L.; Duan, H.T.; Chen, X.L.; Sun, D.Y.; Shi, K. Fifteen-year monitoring of the turbidity dynamics in large lakes and reservoirs in the middle and lower basin of the Yangtze River, China. *Remote Sens. Environ.* **2017**, *190*, 107–121. [CrossRef]
31. Zhu, H.; Zhu, J.S.; Zou, Q. Comprehensive analysis of coordination relationship between water resources environment and high-quality economic development in urban agglomeration in the middle reaches of Yangtze River. *Water* **2020**, *12*, 1301. [CrossRef]

32. Fan, H.M.; Chen, S.S.; Li, Z.E.; Liu, P.X.; Xu, C.Y.; Yang, X.X. Assessment of heavy metals in water, sediment and shellfish organisms in typical areas of the Yangtze River Estuary, China. *Mar. Pollut. Bull.* **2020**, *151*, 110864. [CrossRef] [PubMed]
33. Wei, Q.S.; Wang, B.D.; Zhang, X.L.; Ran, X.B.; Fu, M.Z.; Sun, X.; Yu, Z.G. Contribution of the offshore detached Changjiang (Yangtze River) diluted water to the formation of hypoxia in summer. *Sci. Total Environ.* **2021**, *764*, 142838. [CrossRef]
34. He, G.; Xia, Y.L.; Qin, Y.; Zhu, Y.N.; Wang, W.W. Evaluation and spatial-temporal dynamics change of water resources carrying capacity in the Yangtze River economic belt. *Res. Soil Water Conserv.* **2019**, *26*, 287–300.
35. Yin, H.; Sun, C.; Wang, H.; Qin, Z.D.; Xu, Q.Q.; Ke, G.; Zhao, Q.; Deng, X.W. Water environment issues and pollution prevention strategies in Wuhan reach of Fu River. *Environ. Sci. Manag.* **2018**, *43*, 81–85.
36. Tian, X.J.; Zou, F.; Jin, S.G. Impact of climate change and human activities on water storage changes in the Yangtze River Basin. *J. Geod. Geodyn.* **2019**, *39*, 371–436.
37. Shen, Q.J.; Pei, L.; Zhang, Z.F. Coupling coordination between urbanization and water resources in Yangtze River economic zone. *Resour. Ind.* **2019**, *21*, 1–9.
38. Sadeghi, M.; Babaeian, E.; Tuller, M.; Jones, S.B. The optical trapezoid model: A novel approach to remote sensing of soil moisture applied to Sentinel-2 and Landsat-8 observations. *Remote Sens. Environ.* **2017**, *198*, 52–68. [CrossRef]
39. Zhao, Y.L.; Shen, Q.; Wang, Q.; Yang, F.; Wang, S.L.; Li, J.S.; Zhang, F.F.; Yao, Y. Recognition of Water Colour Anomaly by Using Hue Angle and Sentinel-2 Image. *Remote Sens.* **2020**, *12*, 716. [CrossRef]
40. Zhao, Y.L.; Wang, S.L.; Zhang, F.F.; Shen, Q.; Li, J.S.; Yang, F. Remote Sensing-Based Analysis of Spatial and Temporal Water Colour Variations in Baiyangdian Lake After the Establishment of the Xiong'an New Area. *Remote Sens.* **2021**, *13*, 1729. [CrossRef]
41. Pahlevan, N.; Sarkar, S.; Franz, B.A.; Balasubramanian, S.V.; He, J. Sentinel-2 Multispectral Instrument (MSI) data processing for aquatic science applications: Demonstrations and validations. *Remote Sens. Environ.* **2017**, *201*, 485–497. [CrossRef]
42. Liu, C.D.; He, B.Y.; Li, M.T.; Ren, X.Y. Quantitative modeling of suspended sediment in middle Changjiang River from MODIS. *Chin. Geogr. Sci.* **2006**, *16*, 79–82. [CrossRef]
43. Li, C.; Lian, E.G.; Yang, C.F.; Deng, K.; Qian, P.; Xiao, S.B.; Liu, Z.F.; Yang, S.Y. Seasonal variability of stable isotopes in the Changjiang (Yangtze) River water and its implications for natural climate and anthropogenic impacts. *Environ. Sci. Eur.* **2020**, *32*, 84. [CrossRef]
44. Gong, P.; Liu, H.; Zhang, M.; Li, C.; Wang, J.; Huang, H.; Clinton, N.; Ji, L.; Li, W.; Bai, Y.; et al. Stable classification with limited sample: Transferring a 30m resolution sample set collected in 2015 to mapping 10 m resolution global land cover in 2017. *Sci. Bull.* **2019**, *64*, 370–373. [CrossRef]
45. Wang, X.B.; Xie, S.P.; Zhang, X.L.; Chen, C.; Guo, H.; Du, J.K.; Duan, Z. A robust multi-band water index (MBWI) for automated extraction of surface water from Landsat 8 OLI imagery. *Int. J. Appl. Earth Obs. Geoinf.* **2018**, *68*, 73–91. [CrossRef]
46. Capó, M.; Pérez, A.; Lozano, J.A. An efficient approximation to the k-means clustering for massive data. *Knowl. Based Syst.* **2017**, *117*, 56–69. [CrossRef]
47. CIE (Commission International de l'Eclairage). *Proceedings*; Cambridge University Press: Cambridge, UK, 1931; pp. 19–29.
48. Wang, S.L.; Li, J.S.; Qian, S.; Zhang, B.; Zhang, F.F.; Lu, Z.Y. MODIS- Based radiometric color extraction and classification of inland water with the Forel-Ule scale: A case study of Lake Taihu. *IEEE J. Sel. Top. Appl. Earth Obs. Remote Sens.* **2015**, *8*, 907–918. [CrossRef]
49. Capuzzo, E.; Stephens, D.; Silva, T.; Barry, J.; Forster, R.M. Decrease in water clarity of the Southern and Central North Sea during the 20th-century. *Glob. Chang. Biol.* **2015**, *21*, 2206–2214. [CrossRef]
50. Fleming-Lehtinen, V.; Laamanen, M. Long-term changes in Secchi depth and the role of phytoplankton in explaining light attenuation in the Baltic Sea. *Estuar. Coast. Shelf Sci.* **2012**, *102–103*. [CrossRef]
51. Billah, M.M.; Goodall, J.L. Annual and interannual variations in terrestrial water storage during and following a period of drought in South Carolina, USA. *J. Hydrol.* **2011**, *409*, 472–482. [CrossRef]
52. Peng, T.; Tian, H.; Qin, Z.X.; Wang, G.X. Impacts of climate change and human activities on flow discharge and sediment load in the Yangtze River. *J. Sediment Res.* **2018**, *43*, 54–60.
53. Wang, Y.G.; Shi, H.L.; Liu, Q. Influence of sediment trapping in reservoirs on runoff and sediment discharge variations in Yangtze River. *Adv. Water Sci.* **2014**, *25*, 467–476.
54. Niroumand-Jadidi, M.; Bovolo, F.; Bruzzone, L. Novel Spectral-Derived Features for Empirical Retrieval of Water Quality Parameters: Demonstrations for OLI, MSI, and OLCI Sensors. *IEEE Trans. Geosci. Remote Sens.* **2019**, *57*, 10285–10300. [CrossRef]
55. Gholizadeh, M.H.; Melesse, A.M.; Reddi, L. A Comprehensive Review on Water Quality Parameters Estimation Using Remote Sensing Techniques. *Sensors* **2016**, *16*, 1298. [CrossRef] [PubMed]